NANO LETTERS

Letter

pubs.acs.org/NanoLett

Quantum Interference in Graphene Nanoconstrictions

Pascal Gehring,*[,†] Hatef Sadeghi,[‡] Sara Sangtarash,[‡] Chit Siong Lau,[†] Junjie Liu,[†] Arzhang Ardavan,[§] Jamie H. Warner,[†] Colin J. Lambert,[‡] G. Andrew. D. Briggs,[†] and Jan A. Mol[†]

[†]Department of Materials, University of Oxford, 16 Parks Road, Oxford OX1 3PH, United Kindom

[‡]Quantum Technology Centre, Physics Department, Lancaster University, Lancaster LA1 4YB, United Kingdom

[§]Clarendon Laboratory, Department of Physics, University of Oxford, Parks Road, Oxford OX1 3PU, United Kingdom

Supporting Information

ABSTRACT: We report quantum interference effects in the electrical conductance of chemical vapor deposited graphene nanoconstrictions fabricated using feedback controlled electroburning. The observed multimode Fabry–Pérot interferences can be attributed to reflections at potential steps inside the channel. Sharp antiresonance features with a Fano line shape are observed. Theoretical modeling reveals that these Fano resonances are due to localized states inside the constriction, which couple to the delocalized states that also give rise to the Fabry–Pérot interference patterns. This study provides new insight into the interplay between two fundamental forms of quantum interference in graphene nanoconstrictions.

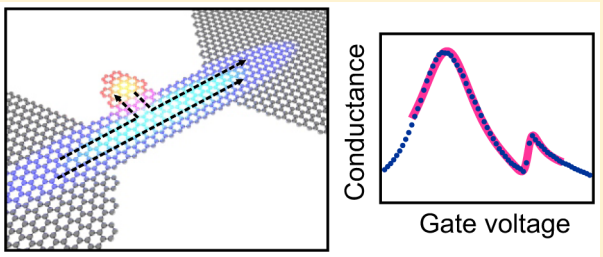

KEYWORDS: *Graphene, quantum interference, Fano resonance, break junction, Fabry–Pérot*

A key feature of electron transport through single molecules and phase-coherent nanostructures is the appearance of transport resonances associated with quantum interference.[1] Examples include Breit–Wigner resonances, multipath Fabry–Pérot resonances, and Fano resonances. Fano resonances can be observed when a localized state interacts with a continuum of extended states and can lead to very steep gradients in the transmission. Unlike Breit–Wigner resonances, they are not lifetime broadened by coupling to the electrodes. The steep slope of Fano resonances makes them attractive for low-power switching and for creating structures with high thermoelectric performance.[2] In what follows, we report the first observation of Fano resonances in electroburnt graphene nanoconstrictions. In addition to these Fano features, the conductance maps exhibit interference patterns, which we attribute to multimode Fabry–Pérot (FP) interferences. Theoretical modeling reveals that the Fano resonances arise from interaction between the delocalized state giving rise to the Fabry–Pérot pattern and a localized state inside the constriction.

Carbon-based nanostructures, such as metallic or semiconducting single carbon chains,[3,4] graphene nanoribbons, and graphene nanoconstrictions are interesting platforms for the study of spintronics[5] and might enable novel technological applications.[6] Graphene nanoconstrictions and nanogaps also provide a robust platform for studying the electric,[7] thermoelectric,[8] and magnetic[9] properties of single molecules. When they are sufficiently narrow, graphene nanoribbons can be used to build field-effect transistors with an on/off ratio that can exceed 1000.[10] In very narrow constrictions, with a width smaller than the electronic wavelength of electrons, quantum interference effects in analogy to subwavelength optics are predicted.[11,12] Graphene nanoconstrictions have been fabricated by means of electron beam lithography,[13] gold break-junction etching masks,[10] local gating,[14] and electroburning of graphene.[15,16] Electroburning has also been used to fabricate graphene quantum dots with addition energies up to 1.6 eV, enabling the observation of Coulomb blockade at room temperature.[17] In this study we use feedback-controlled electroburning to narrow down lithographically defined bowtie shaped graphene constrictions[18] and study their electronic transport behavior.

Our devices are fabricated from single-layer CVD-grown graphene,[19] which we transfer onto a Si/300 nm SiO_2 wafer with prepatterned 10 nm Cr/70 nm Au contacts. We pattern the graphene into a bowtie shape (see Figure 1a,b) using standard electron beam lithography and O_2 plasma etching. The channel length L of the devices and the width W of the narrowest part of the constriction are 4 μm and 200 nm, respectively (see Figure 1a). Our devices are p-doped with a Dirac point V_{Dirac} around 60 V (see Figure 1c). The single-layer nature of the graphene constriction is confirmed by the intensity ratio $I(2D)/I(G) \gg 1$ of the Raman G and 2D peaks (see Figure 1d) and the fact that the 2D peak consists of a single Lorentzian.[20,21] In addition, we observe a D and D′ peak, which we attribute to the defective graphene edges formed during the plasma etching.[21] These defect peaks are not present in bulk single-layer graphene samples.[19] To narrow down the constriction we use a feedback-controlled electroburning

Received: March 14, 2016
Revised: June 12, 2016

DOI: 10.1021/acs.nanolett.6b01104
Nano Lett. XXXX, XXX, XXX–XXX

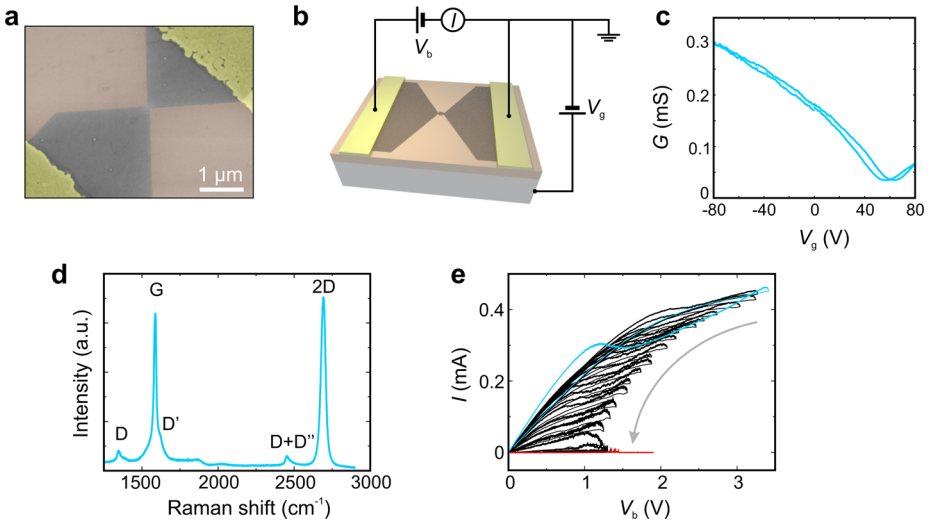

Figure 1. (a) False color SEM image of a graphene constriction (gray) contacted by gold contacts (yellow). (b) Schematic of a graphene nanoconstriction device. (c) Conductance as a function of back gate voltage recorded at V_b = 100 mV of an as-prepared device. (d) Raman spectrum of the center region of the graphene bowtie after electroburing. (e) I–V_b traces recorded during feedback-controlled electroburning. The first and last traces are shown in blue and red, respectively.

technique in air, similar to the one described in ref 18. We ramp-up a voltage applied between the source and drain contact while monitoring the current with a 5 kHz sampling rate (see Figure 1b). As soon as a drop in the current is detected, the voltage is quickly ramped back to zero. This cycle is repeated until the low bias source-drain resistance of the device, which is measured after each burning cycle, exceeds a threshold resistance of 500 MΩ. The feedback conditions are adjusted for each burning cycle depending on the threshold voltage V_{th} at which the drop in the previous cycle occurred. The current–voltage (I–V_b) traces of a typical electroburning process are shown in Figure 1e, where the I–V_b traces before electroburning and after the threshold resistance is reached are colored blue and red, respectively.

During electroburning, the constriction is narrowed down, and as a result, the resistance of the device increases. At the final stage, the (only several atoms wide) constriction can break completely and a nanometer-sized gap is formed.[12] However, for many devices the threshold resistance is reached before a gap is fully formed. In these cases, narrow graphene constrictions or small graphene islands are left between the mesoscopic graphene leads. Graphene quantum dots formed in this manner have been widely studied[15−17,22] as a possible platform for room temperature single-electron transistors. In the following we discuss the details of the transport characteristics of empty graphene nanogaps, quantum dots, and nanoconstrictions recorded at T = 4 K in vacuum (~10^{-6} mbar).

The transport regime, which we attribute to an empty gap, is characterized by low currents and I–V_b characteristics that can be fitted using the standard Simmons model[23] for tunnelling through a single trapezoidal barrier between source and drain (see Figure 2a). In addition, the I–V_b characteristics show no or a relatively small back gate dependence (see Figure 2b). We find gap sizes of 0.5–2.5 nm for these junctions, making them a promising platform for single molecule electronics.[7,24,25]

Devices in the weakly coupled quantum dot regime show suppressed current at low bias (see Figure 2c) and characteristic Coulomb diamonds as a function of bias and gate voltage (see Figure 2d). These transport features are indicative of

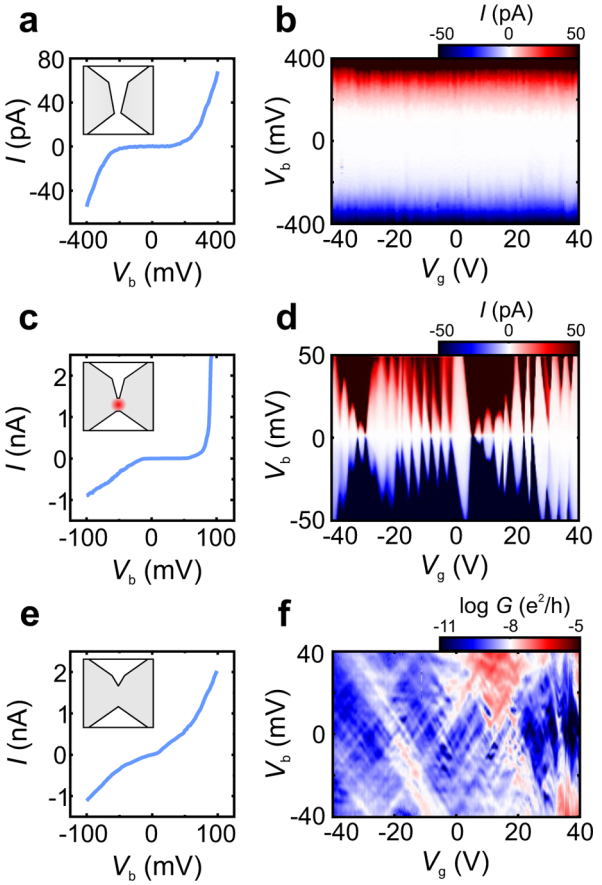

Figure 2. Nanostructures with different electronic behavior formed during electroburning. (a) I–V_b trace and (b) current map of an empty gap. (c) I–V_b trace and (d) current map of a weakly coupled constriction showing sequential tunnelling. (e) I–V_b trace and (f) conductance map of a strongly coupled constriction showing resonance effects. All data was recorded at T = 4 K under vacuum. The insets depict a scheme of the constriction.

sequential electron tunnelling via a weakly coupled quantum dot between source and drain.[26] From the size of the Coulomb

DOI: 10.1021/acs.nanolett.6b01104
Nano Lett. XXXX, XXX, XXX−XXX

diamonds we can extract addition energies for these quantum dots ranging from 20 to 800 meV, comparable to those found by other groups in similar systems.[13,15−17] The formation of graphene quantum dots during electroburning process is the result of electron/hole localization due to charge puddles and/or edge disorder as the graphene channel gets narrower.[27] Theoretical calculations have also shown that localized states can form along the edges of wedge-shaped nanoconstrictions.[28] Furthermore, it is possible that small graphene islands on the order of several nanometers form, which are only weakly coupled to the graphene leads.[17]

The conductance maps of strongly coupled devices are dominated by "chess board"-like interference patterns as shown in Figure 2f. In some samples we could observe a transition from this chess board pattern to a Coulomb diamond regime at high positive gate voltages of $\gtrsim$40 V. This observation is similar to results found in recent studies on short graphene junctions[29,30] and narrow graphene constrictions.[31] In the latter, the chess board pattern was attributed to interference effects of extended states in the source or drain graphene lead connecting the constriction.[31] In general, interference effects occur on a length scale on the order of the phase coherence length but can have different origins. If the transport in the graphene sample is diffusive, i.e., when charge carriers are predominantly scattered at random impurities like edge disorder, point defects, or charge puddles,[27] the origin of the interference pattern is most likely due to quantum interferences of different random scattering paths (universal conductance fluctuations, UCFs). If the channel length is on the order of or shorter than the mean free path of the carriers (quasi-ballistic transport regime), reflections in the channel result in quasi-periodic multimode or collective and periodic single-mode Fabry−Pérot interferences. Carriers can get reflected at the metal contacts[30] or at potential barriers formed by intentional local doping.[32] Whether single- or multimode interference is observed strongly depends on the detailed device geometry.[33]

Fabry−Pérot interference effects have previously been observed in 1D nanowires,[34] carbon nanotubes,[35] and 2D graphene,[30] while UCFs have been observed in mesoscopic single-,[36] bi- and trilayer,[37] and epitaxial graphene samples.[38] To distinguish between these different types of quantum interference, the chess board conductance patterns need to be carefully analyzed for hidden periodicities.[30] From the characteristic energy spacing between single features in the conductance maps and fast Fourier transforms (FFTs) of the data shown in Figure 2f (see Figure S6a,b in the Supporting Information), we can extract a typical energy spacing of 4−5 meV. Using a particle-in-a-box approximation,[30] we estimate the relevant length scale $L = hv_F/(2E)$ to be between 400 nm for the theoretical local density approximation limit of the Fermi velocity of $v_F = 0.8 \times 10^6$ m/s and 1.1 μm for a Fermi velocity of $v_F = 2.4 \times 10^6$ m/s measured for CVD graphene on a quartz substrate.[39] This length scale corresponds to half the minimal distance over which the electrons remain phase coherent; therefore, we can infer a lower bound for the phase coherence length $L_\varphi > 800$ nm in our samples.[29] This value is similar to the value found for exfoliated graphene on SiO_2,[40] epitaxial graphene,[41] and CVD graphene.[42] For short and wide devices small incident angles dominate (longitudinal modes) and resonances appear at $k_F L = n\pi$.[32] However, since our devices are not in the limit $W/L \gg 1$, both longitudinal and transversal modes need to be considered. To model conductance maps for different aspect ratios we have performed nearest-neighbor tight-binding calculations[33] (see section S5 Supporting Information). Our calculations confirm that for $W \gg L$ a periodic interference pattern with high contrast can be observed. This is due to the fact that the energy of transversal modes $E_W = hv_F/(2W)$ gets negligibly small. The same holds for the 1D limit $W \to 0$, where E_W goes to infinity. In both cases the transport is dominated by longitudinal modes only. In the intermediate multimode regime, periodic longitudinal modes can still be observed in the FFT but with much smaller contrast. Since the aspect ratio W/L of our devices is close to unity we expect that the interference pattern shown in Figure 2b will only be quasi-periodic because of multimode interferences. Moreover, the fact that the width W of the samples is not constant will cause the transversal modes to become chaotic.[11]

Because the measured chess board pattern is only quasi-periodic, we cannot exclude UCFs as an origin of the observed pattern. UCFs are normally most pronounced at low doping concentrations when the electrochemical potential of graphene is close to the Dirac point.[30] This is unlikely to be the case in our p-doped graphene junctions. In addition, the periodicity that we can correlate with the geometry of the device is very similar for all devices investigated in this study, which makes multimode Fabry−Pérot interferences a more likely mechanism to explain our data.

Next, we investigate the microscopic origin of the FP reflections. Based on our assumption for the Fermi velocity (see above) we estimate that carriers are coherently reflected on a length scale of $\lesssim$1 μm. The visibility/intensity of FP interferences is determined by the reflectance of the potential steps. Unipolar cavities have a small finesse and result in a small visibility $(G_{max} - G_{min})/(G_{max} + G_{min})$ since the conservation of pseudospin suppresses backscattering in graphene.[32] A smooth bipolar potential step like a pn junction formed near a metal−graphene contact has a much higher finesse and leads to pronounced resonance pattern.[32] However, since the length scale of less than 1 μm found above is much smaller than the channel length of 4 μm of our devices there need to be additional potential steps inside the graphene channel apart from the metal contacts. From scanning electron microscopy and micro Raman spectroscopy (see Sections S1 and S4 in the Supporting Information) we can infer that the local hole concentration within a region of several hundreds of nanometers around the graphene constriction is increased during electroburning. The increase of hole doping of graphene on SiO_2 annealed in air was intensively studied and attributed to doping by O_2 and moisture and a change in the degree of coupling between graphene and SiO_2.[43] This increased p doping can result in the formation of a pp^+p junction in the central region of the devices (see Figure S6c and d in the Supporting Information). Possible resonance conditions are reflections between the gold contact/the pn junction close to the gold contact and the pp^+p junction or reflections within the pp^+p junction, which all have a characteristic length scale of several hundreds of nanometers. This length scale is on the order of the mean free path of charge carriers in our devices (see Supporting Information), which further corroborates our interpretation that the chess board pattern arises from FP interferences rather than scattering at random impurities inside the channel. The visibility of the FP interferences $(G_{max} - G_{min})/(G_{max} + G_{min}) > 10\%$ is high in our devices, which indicates that the unipolar p^+p interfaces need to have a sharp potential drop with $k_F d \ll 1$, where d is the length over which

DOI: 10.1021/acs.nanolett.6b01104
Nano Lett. XXXX, XXX, XXX−XXX

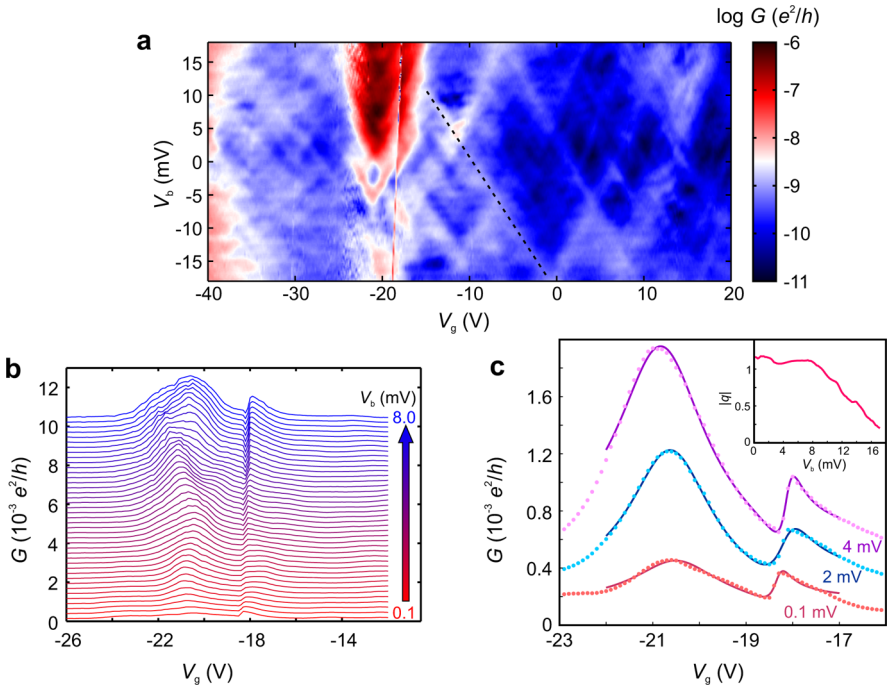

Figure 3. (a) Conductance map at T = 4 K of a strongly coupled constriction showing interference effects. A sharp antiresonance feature around V_g = −18 V can be observed. The dotted line is used to extract the lever arm. (b) Gate traces for different bias voltages 0.1 mV ≤ V_b ≤ 8 mV in 0.2 mV steps of the data shown in (a). The curves are offset by 0.2 × 10^3 e^2/h for clarity. (c) Gate traces at different bias voltages (dotted lines) and fits using eq 1 (solid lines). The inset shows the dependence of the Fano factor |q| as a function of the applied bias voltage.

the carrier density changes.[44] We estimate this length scale by calculating the Fermi vector using $n = k_F^2/\pi$ and the charge carrier concentration $n = C_g^2(V_g - V_{Dirac})^2/e^2$,[30] where C_g is the capacitance of the back gate and e is the elementary charge. For V_{Dirac} = 60 V (see Figure 1c), d is on the order of 3 nm.

We only see interference patterns in nearly fully burned devices and not directly after the first electroburning steps. We attribute this to the decreasing conductance of the graphene constriction during electroburning, which decreases the denominator in $(G_{max} - G_{min})/(G_{max} + G_{min})$ and thus increases the visibility of the interferences. Another possible explanation for the onset of interference pattern after electroburning is the recrystallization of the constriction,[45] which may lead to a higher mean free path that is required for reflections on the micrometer scale. The interplay between reduced width and reduced carrier density may also increase the factor λ/W, where $\lambda = h v_F/E$ is the wavelength of the electrons. If this ratio becomes ≳3−5 the Fabry−Pérot interferences have a high contrast.[11]

We now turn to the sharp antiresonances in the interference regime as shown in Figure 3a,b (around V_g = −18 V) in some samples (see Supporting Information for data of other samples). The slope of this antiresonance feature is different from the slopes of the multimode FP interference patterns. Repeated thermal cycling from 4 K to room temperature did not change the slope and position of the feature observed at 4 K (see Figure S8). The feature consists of an antiresonance/resonance double-peak as shown in Figure 3c. This asymmetric curve has a distinct Fano line shape,[46] which is the result of coherent interaction between a localized resonant state with a delocalized background state.[1] Fano resonances have previously been observed in double donor systems in nanoscale silicon transistors[47] and in bundles of single walled CNTs.[48] Fano resonances are also predicted for single molecule systems, where a backbone state is coupled to the leads, and a pendant side-group is only coupled to the backbone but not to the leads.[1] In a graphene constriction connected to mesoscopic graphene leads there are delocalized states that give rise to the previously discussed FP pattern and bound states, e.g., localized along the edges due to edge roughness, that give rise to Coulomb blockade at high positive gate voltages close to the Dirac point (see Figure 2f).[31] We attribute the observed Fano resonances to the coherent interaction between these states.

To estimate the coherent coupling strength between the localized and delocalized states in the graphene nanoconstriction, we fit the low bias current−gate voltage (I−V_g) traces to the Fano formula:[48,49]

$$G(\varepsilon) = G_{non} + G_{res}\frac{(\varepsilon + q)^2}{\varepsilon^2 + 1} \quad (1)$$

where G_{res} is the coherent contribution to the conductance, q is the complex Fano factor,[50] $\varepsilon = 2(E - \varepsilon_s)/\Gamma_{Fano}$, ε_s and Γ_{Fano} are the energy and coupling strength of the resonant localized state, and G_{non} is the conductance of the nonresonant channel. We model the nonresonant background as the sum of a constant offset G_{off} and a Breit−Wigner peak $A\frac{\Gamma^2}{\Gamma^2 + (E - \varepsilon_b)^2}$. This nonresonant background accounts for the conductance peak close to the observed antiresonance feature. Fits to our data at different bias voltages using eq 1 are shown as solid lines in Figure 3c. We find for a low bias of V_b = 0.1 mV: ε_s = −18.3 meV, Re(q) = 0.3, Im(q) = 1.1, |q| = 1.1, Γ_{Fano} = 0.4 meV and a Breit−Wigner peak at ε_b = −20.5 meV with a coupling strength of Γ = 1.1 meV using a lever arm dE/dV_g of 1 meV/V extracted from the slope of the Fabry−Pérot interference pattern as depicted by the dotted black line in Figure 3a. The Fano factor q is a combined measure for the energetic detuning and the ratio of the transmission amplitudes of the resonant and the

DOI: 10.1021/acs.nanolett.6b01104
Nano Lett. XXXX, XXX, XXX−XXX

nonresonant channel.[49] For $q \to \infty$, the transport is dominated by the resonant channel and the line shape becomes that of a Breit–Wigner peak. For $q \to 0$ nonresonant transport dominates resulting in a symmetric dip in the conductance.[49] The value of $|q| = 1.1$ found in our experiments results in an asymmetric feature with characteristic Fano line-shape.[48] The width of $\Gamma_{Fano} = 0.4$ meV of the resonant state is similar to the values of 0.25–0.5 meV found for carbon nanotube bundles.[48] The Fano factor q decreases with increasing positive bias voltage (see inset in Figure 3c), which we attribute to a detuning of the energies of the localized state and the extended states. For large negative bias voltages the detuning changes the Fano factor from 1 to a high value, and the transport is dominated by a resonant channel resulting in a Breit–Wigner peak.

The slope of the Fano feature, as seen in Figure 3a, results from the electrostatic coupling of the localized "pendant" state to the gate and lead electrodes. Figure 4a shows a tight-binding model of a pendant state interacting with an extended "backbone" state. A chain of five sites acts as the backbone, while a single site coupled to the second site of the backbone serves as pendant group. Figure 4b shows the calculated transmission coefficient $T(E)$ as a function of energy E. A Fano-resonance appears at an energy of about 0.5 eV, which is associated with the site energy of the bound state. The various transmission maxima are Fabry–Pérot resonances of the backbone channel. To calculate the differential conductance characteristic $dI/dV_b(V_b, V_g)$ of the device for different gate voltages V_g, bias- and gate voltage-dependent transmission coefficients $T(E, V_b, V_g)$ were calculated for two different potential profiles, where (i) the bias drops over the left and right contacts (Figure 4c); or (ii) the bias drops along the device channel (Figure 4d). In the case where the bias voltage drops across the contacts (see Figure 4c), the on-site energies of the pendant group and the backbone are not influenced by the applied bias voltage. As a consequence the two antiresonance Fano lines have the same slope as the Fabry–Pérot interference lines (see Figure 4e). In contrast, when the potential drops over the channel (see Figure 4d), the slopes of the antiresonance lines and the backbone resonances become different (see Figure 4f). As a result of the asymmetry of the junction, one of the Fano lines almost vanishes (see section S7 in the Supporting Information for details). Comparing the calculations in Figure 4e,f with the experimental data in Figure 3a, we can conclude that, first, the investigated junctions are asymmetric and, second, that a considerable portion of the applied voltage has to drop across the junction. In a more realistic model, where two hexagonal lattices are connected to various scattering regions with and without pendant groups (see Figure 5), Fano resonances can be only observed in junctions with pendant groups (see Sections S6 and S8 in the Supporting Information for more details). Molecular-dynamics simulations and density functional theory calculations of different atomic configurations during nanogap formation[12]

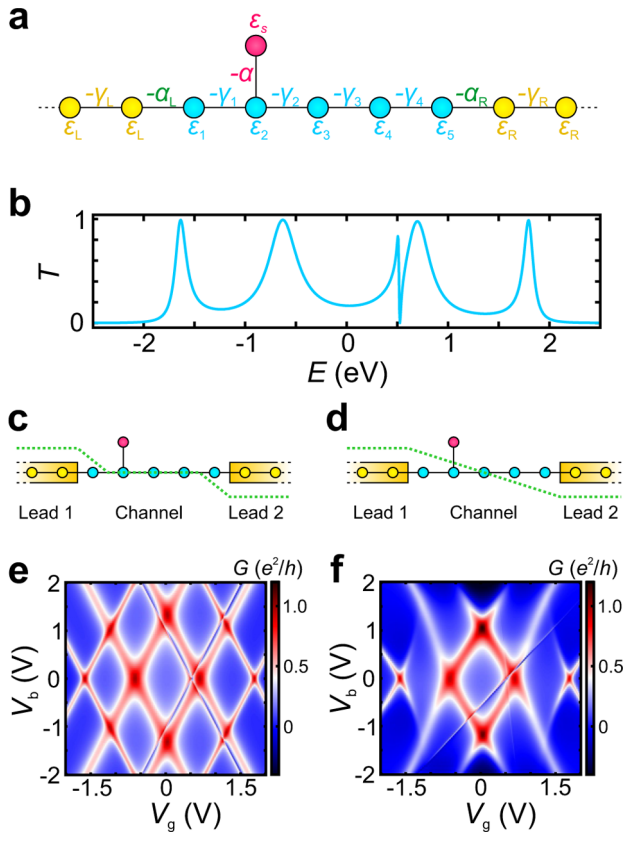

Figure 4. (a) Tight-binding model of a pendant state interacting with an extended "backbone" state. The backbone is described by a chain of five sites with on-site energies ε_{1-5} that are coupled by hopping matrix elements, γ_{1-4}, and coupled to the leads via the outermost sites by hopping matrix elements, α_L (on the left side) and β_R (on the right side). The pendant group with an on-site energy ε_s is coupled to the second site of the backbone by a hopping matrix element, α. (b) Calculated transmission coefficient as a function of energy. (c,d) Sketch of the potential profile where (c) the bias drops over the left and right contacts and (d) the bias voltage drops along the device channel. (e,f) Corresponding conductance maps as a function of bias and gate voltage for the cases depicted in (c,d), respectively.

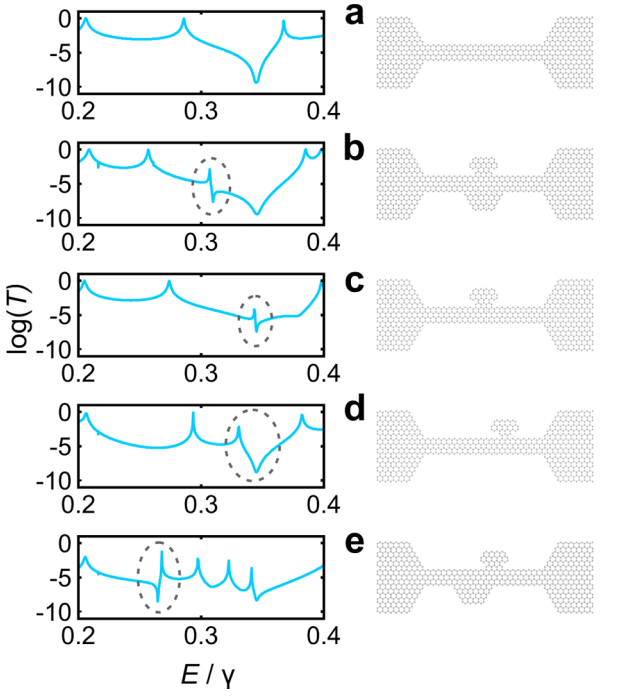

Figure 5. Transmission through graphene junctions. (a) Clean graphene ribbon connected to two graphene electrodes; (b–e) graphene junctions with different shape and position of pendent groups. The dotted circles indicate the position of Fano features.

DOI: 10.1021/acs.nanolett.6b01104
Nano Lett. XXXX, XXX, XXX–XXX

further show that dangling carbon atoms and edge disorder can lead to Fano resonance in the transmission spectra of partially burned graphene nanogaps (see Section S8 in the Supporting Information).

In summary we investigated graphene nanoconstrictions fabricated by narrowing down bowtie shaped graphene ribbons using a feedback controlled electroburning technique. In the case of weakly coupled constrictions, the transport is dominated by Coulomb blockade with addition energies up to 800 meV. In the strongly coupled regime, we observe quasi-periodic chess board like pattern in the conductance maps, which we attribute to multimode Fabry–Pérot interferences of delocalized states whose length scale agrees with two possible resonance conditions: reflections inside the current-annealed highly doped part of the device or reflections between the electrical contacts and the highly doped part. In some of the devices, we observe sharp antiresonance features with a Fano line shape inside the interference regime in agreement with our theoretical modeling. We attribute these features to interferences between the extended states and localized states inside the constriction. Such sharp antiresonances have the potential to underpin the development of low-power switches because the transmission of the structure can be tuned by a small gate voltage. Moreover, the Mott formula predicts that a high $d\ln G/dV_g$ should also result in a high Seebeck coefficient,[51] making such devices promising candidates for thermoelectric energy harvesting.

■ ASSOCIATED CONTENT

Supporting Information

The Supporting Information is available free of charge on the ACS Publications website at DOI: 10.1021/acs.nanolett.6b01104.

SEM images of the devices, electrical characterization of graphene used in this study, micro-Raman data, detailed study of interference pattern, additional Fano data, bias dependence of the Fano feature, molecular dynamics simulations (PDF)

■ AUTHOR INFORMATION

Corresponding Author

*E-mail: pascal.gehring@materials.ox.ac.uk.

Notes

The authors declare no competing financial interest.

■ ACKNOWLEDGMENTS

We thank the Royal Society for a Newton International Fellowship for J.A.M., the Agency for Science Technology and Research (A*STAR) for a studentship for C.S.L., and a University Research Fellowship for J.H.W. This work is supported by Oxford Martin School, the European Commission (EC) FP7 ITN "MOLESCO" (project no. 606728) and UK EPSRC (grant nos. EP/K001507/1, EP/J014753/1, EP/H035818/1 and EP/J015067/1). This project/publication was made possible through the support of a grant from Templeton World Charity Foundation. The opinions expressed in this publication are those of the author(s) and do not necessarily reflect the views of Templeton World Charity Foundation. The authors would like to thank D. Gunlycke for his help and the useful discussions, Y. Fan and J. Nägele for providing supporting transport data, and H. Tan for providing CVD graphene.

■ REFERENCES

(1) Lambert, C. J. *Chem. Soc. Rev.* **2015**, *44*, 875–888.
(2) Finch, C. M.; Garcia-Suarez, V. M.; Lambert, C. J. *Phys. Rev. B: Condens. Matter Mater. Phys.* **2009**, *79*, 033405.
(3) Rong, Y. M.; Warner, J. H. *ACS Nano* **2014**, *8*, 11907–11912.
(4) Chuvilin, A.; Meyer, J. C.; Algara-Siller, G.; Kaiser, U. *New J. Phys.* **2009**, *11*, 083019.
(5) Son, Y. W.; Cohen, M. L.; Louie, S. G. *Nature* **2006**, *444*, 347–349.
(6) Pezoldt, J.; Hummel, C.; Hanisch, A.; Hotovy, I.; Kadlecikova, M.; Schwierz, F. *Phys. Status Solidi C* **2010**, *7*, 390–393.
(7) Mol, J. A.; Lau, C. S.; Lewis, W. J. M.; Sadeghi, H.; Roche, C.; Cnossen, A.; Warner, J. H.; Lambert, C. J.; Anderson, H. L.; Briggs, G. A. D. *Nanoscale* **2015**, *7*, 13181–13185.
(8) Sadeghi, H.; Sangtarash, S.; Lambert, C. J. *Beilstein J. Nanotechnol.* **2015**, *6*, 1413–1420.
(9) Candini, A.; Klyatskaya, S.; Ruben, M.; Wernsdorfer, W.; Affronte, M. *Nano Lett.* **2011**, *11*, 2634–2639.
(10) Lu, Y.; Goldsmith, B.; Strachan, D. R.; Lim, J. H.; Luo, Z. T.; Johnson, A. T. C. *Small* **2010**, *6*, 2748–2754.
(11) Darancet, P.; Olevano, V.; Mayou, D. *Phys. Rev. Lett.* **2009**, *102*, 136803.
(12) Sadeghi, H.; Mol, J. A.; Lau, C. S.; Briggs, G. A. D.; Warner, J.; Lambert, C. J. *Proc. Natl. Acad. Sci. U. S. A.* **2015**, *112*, 2658–2663.
(13) Ihn, T.; Guttinger, J.; Molitor, F.; Schnez, S.; Schurtenberger, E.; Jacobsen, A.; Hellmuller, S.; Frey, T.; Droscher, S.; Stampfer, C.; Ensslin, K. *Mater. Today* **2010**, *13*, 44–50.
(14) Allen, M. T.; Martin, J.; Yacoby, A. *Nat. Commun.* **2012**, *3*, 934.
(15) Moser, J.; Bachtold, A. *Appl. Phys. Lett.* **2009**, *95*, 173506.
(16) Ki, D. K.; Morpurgo, A. F. *Phys. Rev. Lett.* **2012**, *108*, 266601.
(17) Barreiro, A.; van der Zant, H. S. J.; Vandersypen, L. M. K. *Nano Lett.* **2012**, *12*, 6096–6100.
(18) Lau, C. S.; Mol, J. A.; Warner, J. H.; Briggs, G. A. D. *Phys. Chem. Chem. Phys.* **2014**, *16*, 20398–20401.
(19) Wu, Y. M. A.; Fan, Y.; Speller, S.; Creeth, G. L.; Sadowski, J. T.; He, K.; Robertson, A. W.; Allen, C. S.; Warner, J. H. *ACS Nano* **2012**, *6*, 5010–5017.
(20) Sun, Z. Z.; Yan, Z.; Yao, J.; Beitler, E.; Zhu, Y.; Tour, J. M. *Nature* **2010**, *468*, 549–552.
(21) Ferrari, A. C.; Basko, D. M. *Nat. Nanotechnol.* **2013**, *8*, 235–246.
(22) Puczkarski, P.; Gehring, P.; Lau, C. S.; Liu, J. J.; Ardavan, A.; Warner, J. H.; Briggs, G. A. D.; Mol, J. A. *Appl. Phys. Lett.* **2015**, *107*, 133105.
(23) Simmons, J. G. *J. Appl. Phys.* **1963**, *34*, 1793–1803.
(24) Lau, C. S.; Sadeghi, H.; Rogers, G.; Sangtarash, S.; Dallas, P.; Porfyrakis, K.; Warner, J.; Lambert, C. J.; Briggs, G. A. D.; Mol, J. A. *Nano Lett.* **2016**, *16*, 170–176.
(25) Burzurí, E.; Island, J. O.; Díaz-Torres, R.; Fursina, A.; González-Campo, A.; Roubeau, O.; Teat, S. J.; Aliaga-Alcalde, N.; Ruiz, E.; van der Zant, H. S. J. *ACS Nano* **2016**, *10*, 2521–2527.
(26) Hanson, R.; Kouwenhoven, L. P.; Petta, J. R.; Tarucha, S.; Vandersypen, L. M. K. *Rev. Mod. Phys.* **2007**, *79*, 1217–1265.
(27) Bischoff, D.; Varlet, A.; Simonet, P.; Eich, M.; Overweg, H. C.; Ihn, T.; Ensslin, K. *Appl. Phys. Rev.* **2015**, *2*, 031301.
(28) Muñoz-Rojas, F.; Jacob, D.; Fernández-Rossier, J.; Palacios, J. J. *Phys. Rev. B: Condens. Matter Mater. Phys.* **2006**, *74*, 195417.
(29) Miao, F.; Wijeratne, S.; Zhang, Y.; Coskun, U. C.; Bao, W.; Lau, C. N. *Science* **2007**, *317*, 1530–1533.
(30) Oksanen, M.; Uppstu, A.; Laitinen, A.; Cox, D. J.; Craciun, M. F.; Russo, S.; Harju, A.; Hakonen, P. *Phys. Rev. B: Condens. Matter Mater. Phys.* **2014**, *89*, 121414.
(31) Bischoff, D.; Libisch, F.; Burgdorfer, J.; Ihn, T.; Ensslin, K. *Phys. Rev. B: Condens. Matter Mater. Phys.* **2014**, *90*, 115405.
(32) Rickhaus, P.; Maurand, R.; Liu, M. H.; Weiss, M.; Richter, K.; Schonenberger, C. *Nat. Commun.* **2013**, *4*, 2342.
(33) Gunlycke, D.; White, C. T. *Appl. Phys. Lett.* **2008**, *93*, 122106.
(34) Kretinin, A. V.; Popovitz-Biro, R.; Mahalu, D.; Shtrikman, H. *Nano Lett.* **2010**, *10*, 3439–3445.

DOI: 10.1021/acs.nanolett.6b01104
Nano Lett. XXXX, XXX, XXX–XXX

(35) Liang, W. J.; Bockrath, M.; Bozovic, D.; Hafner, J. H.; Tinkham, M.; Park, H. *Nature* **2001**, *411*, 665−669.
(36) Morozov, S. V.; Novoselov, K. S.; Katsnelson, M. I.; Schedin, F.; Ponomarenko, L. A.; Jiang, D.; Geim, A. K. *Phys. Rev. Lett.* **2006**, *97*, 016801.
(37) Staley, N. E.; Puls, C. P.; Liu, Y. *Phys. Rev. B: Condens. Matter Mater. Phys.* **2008**, *77*, 155429.
(38) Berger, C.; Song, Z. M.; Li, X. B.; Wu, X. S.; Brown, N.; Naud, C.; Mayou, D.; Li, T. B.; Hass, J.; Marchenkov, A. N.; Conrad, E. H.; First, P. N.; de Heer, W. A. *Science* **2006**, *312*, 1191−1196.
(39) Hwang, C.; Siegel, D. A.; Mo, S. K.; Regan, W.; Ismach, A.; Zhang, Y. G.; Zettl, A.; Lanzara, A. *Sci. Rep.* **2012**, *2*, 590.
(40) Lee, G. H.; Jeong, D.; Choi, J. H.; Doh, Y. J.; Lee, H. J. *Phys. Rev. Lett.* **2011**, *107*, 146605.
(41) Lara-Avila, S.; Tzalenchuk, A.; Kubatkin, S.; Yakimova, R.; Janssen, T. J. B. M.; Cedergren, K.; Bergsten, T.; Fal'ko, V. *Phys. Rev. Lett.* **2011**, *107*, 166602.
(42) Baker, A. M. R.; Alexander-Webber, J. A.; Altebaeumer, T.; Janssen, T. J. B. M.; Tzalenchuk, A.; Lara-Avila, S.; Kubatkin, S.; Yakimova, R.; Lin, C. T.; Li, L. J.; Nicholas, R. J. *Phys. Rev. B: Condens. Matter Mater. Phys.* **2012**, *86*, 235441.
(43) Ryu, S.; Liu, L.; Berciaud, S.; Yu, Y. J.; Liu, H. T.; Kim, P.; Flynn, G. W.; Brus, L. E. *Nano Lett.* **2010**, *10*, 4944−4951.
(44) Cheianov, V. V.; Fal'ko, V. I. *Phys. Rev. B: Condens. Matter Mater. Phys.* **2006**, *74*, 041403.
(45) Qi, Z. J.; Daniels, C.; Hong, S. J.; Park, Y. W.; Meunier, V.; Drndic, M.; Johnson, A. T. C. *ACS Nano* **2015**, *9*, 3510−3520.
(46) Miroshnichenko, A. E.; Flach, S.; Kivshar, Y. S. *Rev. Mod. Phys.* **2010**, *82*, 2257−2298.
(47) Verduijn, J.; Tettamanzi, G. C.; Lansbergen, G. P.; Collaert, N.; Biesemans, S.; Rogge, S. *Appl. Phys. Lett.* **2010**, *96*, 072110.
(48) Babić, B.; Schönenberger, C. *Phys. Rev. B: Condens. Matter Mater. Phys.* **2004**, *70*, 195408.
(49) Gores, J.; Goldhaber-Gordon, D.; Heemeyer, S.; Kastner, M. A.; Shtrikman, H.; Mahalu, D.; Meirav, U. *Phys. Rev. B: Condens. Matter Mater. Phys.* **2000**, *62*, 2188−2194.
(50) Clerk, A. A.; Waintal, X.; Brouwer, P. W. *Phys. Rev. Lett.* **2001**, *86*, 4636−4639.
(51) Cutler, M.; Mott, N. F. *Phys. Rev.* **1969**, *181*, 1336−1340.

DOI: 10.1021/acs.nanolett.6b01104
Nano Lett. XXXX, XXX, XXX−XXX